

Structural, Optical and Multiferroic Properties of BiFeO₃ Nanoparticles Synthesized by Soft Chemical Route

Manisha Arora · P.C. Sati · Sunil Chauhan ·
Sandeep Chhoker · A.K. Panwar · Manoj Kumar

Received: 27 July 2012 / Accepted: 21 August 2012 / Published online: 5 September 2012
© Springer Science+Business Media, LLC 2012

Abstract BiFeO₃ nanoparticles were prepared via a soft chemical method using citric acid and tartaric acid routes followed by calcination at low temperature. Structural characterization showed remarkably different conditions for pure phase formation from both routes. The tartaric acid route was effective in obtaining pure phase BiFeO₃ nanoparticles while citric acid route required leaching in dilute nitric acid to remove impurity phases. Further optical, magnetic, and dielectric characterizations of pure phase BiFeO₃ nanoparticles obtained by tartaric acid route were done. X-ray diffraction and Raman spectroscopy confirmed the distorted rhombohedral structure of BiFeO₃ nanoparticles. The average crystallite size of BiFeO₃ nanoparticles was found to vary in the range 30–50 nm. Fourier Transformed Infrared spectra of BiFeO₃ samples calcined at different temperatures were studied in order to analyze various bond formations in the samples. UV-Visible diffuse absorption showed that BFO nanoparticles strongly absorb visible light in the wavelength region of 400–580 nm with absorption cut-off wavelength of 571 nm. The band gap of BiFeO₃ nanoparticles was found to be 2.17 eV as calculated from absorption coefficient spectra. Magnetic measurement showed saturated hysteresis loop indicating ferromagnetic behavior of BiFeO₃ nanoparticles at room temperature. Temperature dependent dielectric constant showed anomaly well below the antiferromagnetic Néel temperature indicating decrease

in antiferromagnetic Néel temperature of BiFeO₃ nanoparticles.

Keywords Bismuth ferrite · Nanoparticles · Optical property · Magnetism

1 Introduction

Materials that possess electric and magnetic ordering simultaneously in the same phase are known as multiferroics. These materials can exhibit magnetoelectric (ME) effect i.e. induction of magnetization by electric field or of polarization by magnetic field at room temperature. Multiferroic materials have become the topic of great interest to the researchers because of its applications in various fields of electrical, magnetic and optical devices [1, 2]. BiFeO₃ (BFO) is the most studied multiferroic material due to the existence of both ferroelectric and (anti) ferromagnetic ordering in the same phase above room temperature. BiFeO₃ possesses distorted rhombohedral structure with Curie temperature $T_c \sim 1100$ K and magnetic ordering is G type antiferromagnetic with Néel temperature $T_N \sim 640$ K [3]. The magnetic structure of BiFeO₃ is spatially modulated with a cycloid spin structure with period 620 Å in which all magnetic spins are oriented antiparallel to each other resulting in no magnetization at room temperature [4]. Further it is very difficult to synthesize single phase BiFeO₃ because of the very narrow range of the synthesis temperature for phase stability. However, decrease in particle size below 62 nm gives rise to suppression of spiral structure which improves magnetization in BFO [5]. Modern synthesis techniques such as solid state route, sol gel technique and sonochemical route have been applied to obtain pure phase BFO [6–8].

In addition to multiferroic properties, BFO has potential to be used in variety of devices because of its interesting op-

M. Arora · P.C. Sati · S. Chauhan · S. Chhoker · M. Kumar (✉)
Department of Physics and Materials Science and Engineering,
Jaypee Institute of Information Technology, Noida 201307, India
e-mail: manoj.chauhan@jiit.ac.in

A.K. Panwar
Department of Applied Physics, Delhi Technological University,
Delhi 110042, India

tical properties in visible region. It can be used as a photocatalytic material due to its narrow band gap which allows carrier excitation, especially in commercially available femto second laser pulses [9]. Recently the photocatalytic properties of BFO powders under visible light illumination have been reported [10]. Gao et al. also suggested that BFO nanowires might also be useful for photocatalytic decomposition of organic contaminants [11]. Apart from all these applications photocatalytic properties of BFO degraded due to the presence of impurity phases and structure instability. In the present communication we compared citric acid and tartaric acid routes of sol gel technique to obtain phase pure BFO nanoparticles. Further detailed structural, optical, magnetic and dielectric properties of BFO nanoparticles are reported in this paper.

2 Experimental Details

BFO nanoparticles were synthesized by metal ions complexing with citric acid and tartaric acid using soft chemical route. For the synthesis of BFO powder from citric acid, $\text{Bi}(\text{NO}_3)_3 \cdot 5\text{H}_2\text{O}$, $\text{Fe}(\text{NO}_3)_3 \cdot 9\text{H}_2\text{O}$, citric acid and ethylene glycol were used to prepare precursor solution. An aqueous solution of citric acid was prepared in distilled water and then $\text{Bi}(\text{NO}_3)_3 \cdot 5\text{H}_2\text{O}$ and $\text{Fe}(\text{NO}_3)_3 \cdot 9\text{H}_2\text{O}$ were added with constant stirring at 50–60 °C followed by addition of ethylene glycol to the solution with citric acid/ethylene glycol proportion (70:30). The solution was heated at 100 °C on hot plate until gel formation occurs after evaporation of water. The dried powder was then sintered at 550 °C for 2 hrs to get desired phase of BFO nanoparticles. On the other hand, synthesis of BFO powder by tartaric acid route involved tartaric acid as a template material and dilute nitric acid as oxidizing agent. Stoichiometric amount of $\text{Bi}(\text{NO}_3)_3 \cdot 5\text{H}_2\text{O}$ (Sigma Aldrich, 98 %) and $\text{Fe}(\text{NO}_3)_3 \cdot 9\text{H}_2\text{O}$ (Sigma Aldrich, 98 %) were dissolved in deionized water along with small amount of dilute nitric acid. This was followed by addition of tartaric acid (ratio of tartaric acid and metal nitrates was 1:2 mole). This solution was heated up to 60 °C for 12 hrs with constant stirring followed by heat treatment in an oven for 4–5 hrs in order to obtain fluffy light yellow color gel. The dried powder was calcined at 550 °C for 2 hrs in order to get crystalline phase. After the heat treatment, samples were characterized by X-ray diffraction (XRD) using Panalytical X'Pert Pro X-ray diffractometer. Rietveld Refinement was carried out to find various structural parameters. Transmission electron microscopy (Philips CM 10) was used to study the particle size. Fourier Transform infrared (FTIR) spectra were obtained (Perkin Elmer Spectrum BS-III) at a resolution of 4 cm^{-1} using a photo detector. Optical properties were studied by using UV–Visible diffuse reflectance (Ocean optics

UV–Visible 4000). Magnetization measurements were taken on Lake shore Vibrating Sample Magnetometer (VSM). The dielectric measurements were carried on silver coated pellets in the temperature range 40–450 °C at various frequencies.

3 Results and Discussion

Figure 1 shows XRD patterns of BFO nanoparticles (sintered at 550 °C) prepared by sol gel method via citric and tartaric acid routes, respectively. It can be seen in Fig. 1(a) that majority of the peaks belong to distorted rhombohedral structure of BiFeO_3 along with some impurity peaks of $\text{Bi}_{36}\text{Fe}_{24}\text{O}_{57}$ and $\text{Bi}_2\text{Fe}_4\text{O}_9$ for sample prepared by citric acid route. Leaching was done in dilute nitric acid to remove impurity phases present in BFO powder prepared by citric acid route. Figure 1(b) shows XRD pattern of BFO nanoparticles prepared by citric acid route after leaching in dilute nitric acid. Leaching was effective in reducing impurity phases; however, few impurity peaks still appeared in the XRD pattern. On the contrary, we obtained pure phase BFO nanoparticles via tartaric acid route (Fig. 1(c)) even without leaching in dilute nitric acid. Further characterizations of BFO nanoparticles prepared by tartaric acid route were done and discussed in this paper. All XRD peaks for sample prepared by tartaric acid route has been indexed according to rhombohedrally distorted perovskite structure with space group $R3c$. Rietveld Refinement of XRD pattern of BFO nanoparticles prepared by tartaric acid route has been performed to investigate various structural parameters. The lattice parameters and unit cell volume were calculated as $a = b = 5.5785 \text{ \AA}$, $c = 13.8654 \text{ \AA}$ and $373.6829 (\text{ \AA})^3$, respectively. The difference in the experimental and simulated data is shown in Fig. 1(d). It was observed from fitting parameters that the structure is very well fitted for rhombohedral system where the weight pattern factor R_{wp} and the expected pattern factor R_{exp} are 14.2 and 20.6, respectively. The average crystallite size as calculated using Debye-Scherrer formula was found to be 40 nm assuming that small crystallite size to be the only reason for line broadening of XRD peaks.

To investigate the particle size and morphology of the nanoparticles, transmission electron microscopy (TEM) was performed using carbon coated copper grid. Figure 2(a) shows the TEM image for BFO nanoparticles with particle size varying from 30–50 nm with quasi spherical morphology. Figure 2(b) shows the selected area electron diffraction (SAED) pattern taken from Fig. 2(a). The well resolved electron diffraction spots confirmed the highly polycrystalline nature of BFO nanoparticles. The observed lattice spacing is measured to be 3.9 Å, 2.7 Å, 2.2 Å and 1.9 Å which correspond to (012), (110), (202) and (024) lattice planes of BFO, respectively.

Fig. 1 (a) XRD patterns of BFO nanoparticles prepared by Citric acid route and (b) followed by leaching. (c) XRD pattern of BFO nanoparticles prepared by tartaric acid route and (d) Rietveld refinement of XRD pattern of BFO nanoparticles prepared by Tartaric acid route

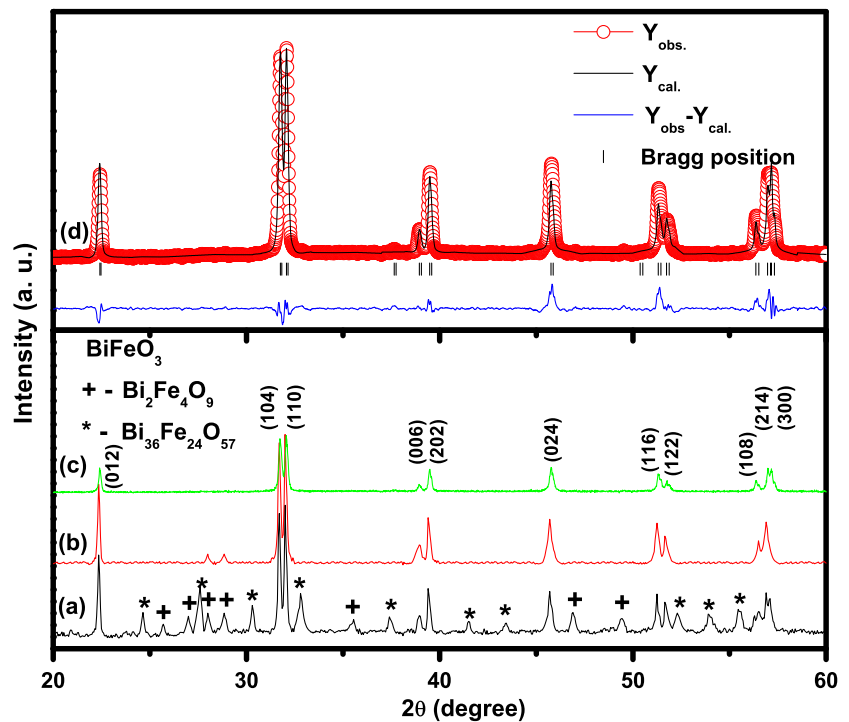
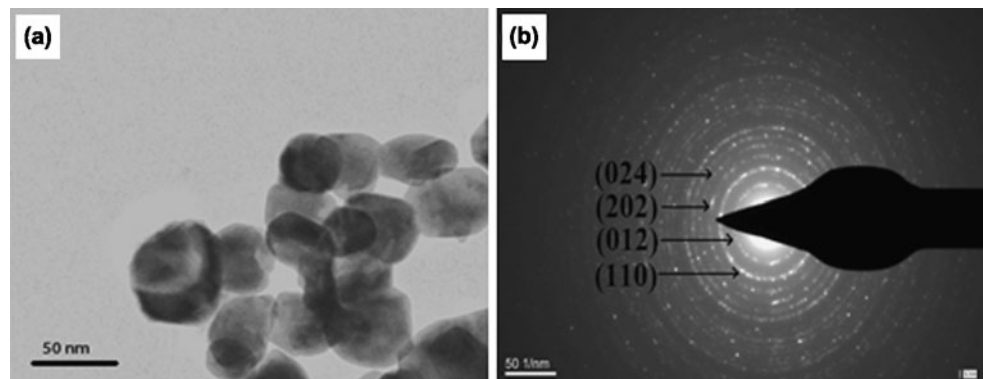


Fig. 2 (a) TEM image of BFO nanoparticles, (b) SAED pattern of BFO nanoparticles



Further Raman spectroscopy was used to study the structural characteristics of BFO nanoparticles prepared by tartaric acid route. More often, 13 Raman active modes ($4A_1 + 9E$) for BFO having distorted rhombohedral structure with $R3c$ space group are observed. The room temperature Raman spectrum of BFO nanoparticles is shown in Fig. 3(a). Here we fitted 10 Raman modes in the range $100\text{--}700\text{ cm}^{-1}$. Three intense peak at 136 cm^{-1} , 170 cm^{-1} and 217 cm^{-1} and a weak intensity peak at 475 cm^{-1} are assign to A_{11} , A_{12} , A_{13} and A_{14} modes, respectively. The peaks around 260 cm^{-1} , 278 cm^{-1} , 345 cm^{-1} , 365 cm^{-1} , 469 cm^{-1} and 520 cm^{-1} are assigned to E_1 , E_2 , E_3 , E_4 , E_5 , and E_6 modes, respectively. Raman spectrum of BFO nanoparticles is in good agreement with previous reports on single crystal BFO [12] and thin film BFO [13] as shown in Table 1.

Figure 3(b) shows FTIR spectra of BFO nanoparticles (sintered at $250\text{ }^\circ\text{C}$, $350\text{ }^\circ\text{C}$, $450\text{ }^\circ\text{C}$ and $550\text{ }^\circ\text{C}$) in the wave

number range $1000\text{--}400\text{ cm}^{-1}$. It is clear that BFO nanoparticles sintered at $250\text{ }^\circ\text{C}$ and $350\text{ }^\circ\text{C}$ did not show any absorption indicating the absence of bond formation. However, the sample sintered at $450\text{ }^\circ\text{C}$ showed two weak broad absorption peaks around 450 cm^{-1} and 550 cm^{-1} , respectively. On further increasing the sintering temperature, intensity of broad absorption peaks increases indicating the completion of bond formation and high degree of crystallization. The broad absorption peaks at 550 cm^{-1} and 440 cm^{-1} are due to overlapping of Fe–O and Bi–O group vibration. Absorption peaks at 550 cm^{-1} and 440 cm^{-1} are the characteristics of Fe–O stretching and bending vibrations of octahedral FeO_6 group, respectively [14]. BiO_6 octahedral structure unit also possesses absorption peaks at 525 cm^{-1} and 450 cm^{-1} [15]. Peak corresponding to 667 cm^{-1} is attributed to water absorption from environment. As the calcination temperature increases these peaks becomes promi-

Fig. 3 (a) Raman spectra of BFO nanoparticles, (b) FTIR spectra of BFO nanoparticles sintered at different temperatures, (c) UV–Visible absorption spectra of BFO nanoparticles and (d) the plot between $(\alpha h\nu)^2$ and binding energy for BFO nanoparticles

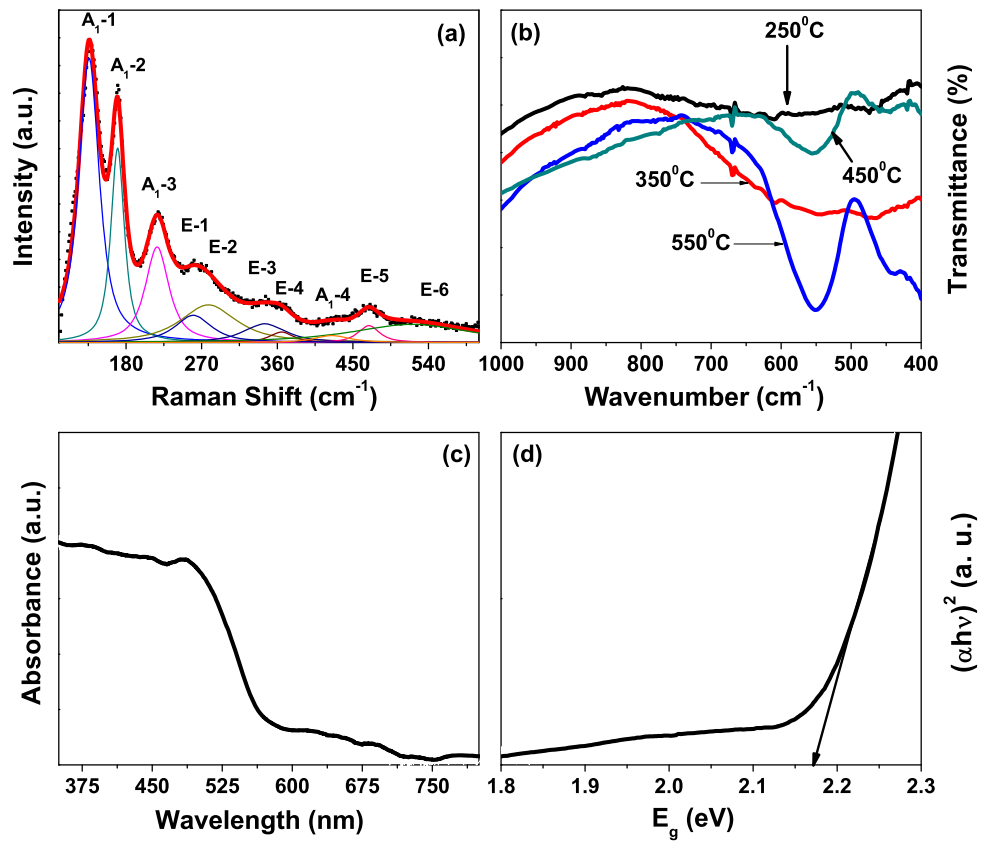


Table 1 Comparison of Raman Mode positions (cm^{-1}) in our study with the reported data on single crystal BFO by Fukumura et al. [12] and data on thin film of BFO by Singh et al. [13]

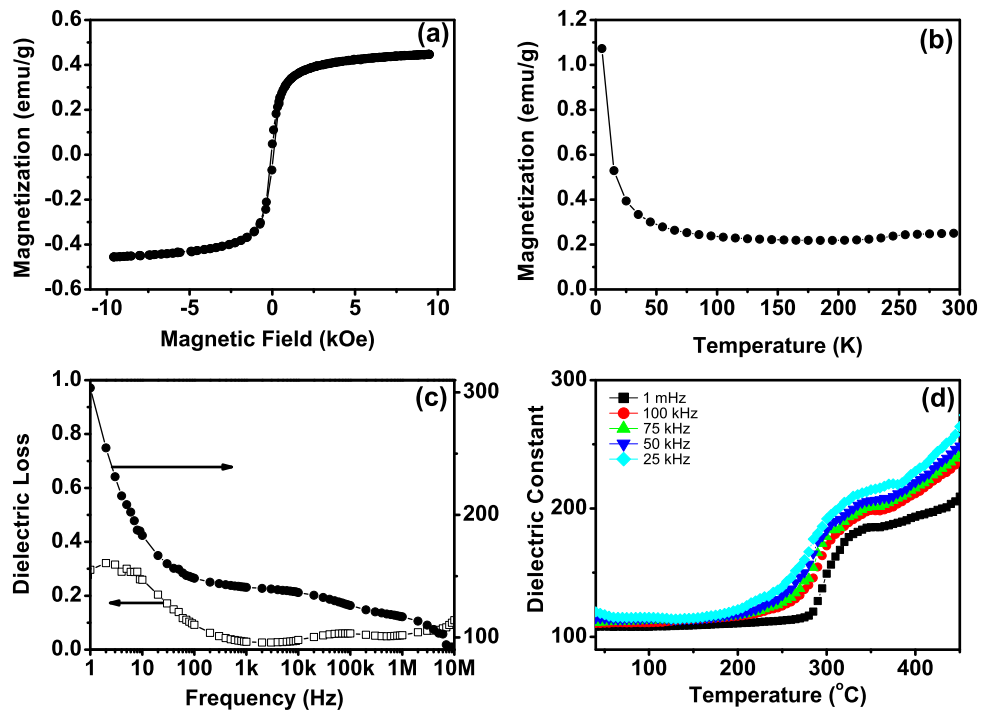
Raman modes	Our study (cm^{-1})	Fukumura et al. (cm^{-1})	Singh et al. (cm^{-1})
A ₁ -1	136	147	136
A ₁ -2	170	176	168
A ₁ -3	217	227	211
A ₁ -4	425	490	425
E-1	260	265	275
E-2	278	279	335
E-3	345	351	365
E-4	365	375	456
E-5	469	437	549
E-6	520	525	597

ment which confirms the Bi–O and Fe–O bonds formation at 550 °C.

BFO is a small band gap metal oxide semiconductor which is very useful as a visible light irradiated photocatalyst. In order to examine the optical properties of BFO, optical response such as the absorption from BFO nanoparticles were observed. Figure 3(c) shows UV–Visible absorption spectra in the range of 350–800 nm for BFO nanoparticles in the diffuse reflectance mode. It is observed that the absorption spectrum of BFO nanoparticles features three unambiguous absorption regions. The broad absorption band from 450–600 nm confirmed that BFO nanoparticles can

absorb higher percentage of visible light. This absorption band arises due to two types of electronic transition. The first excitation is due to electronic transitions from 6A_1 state to ${}^4T_1({}^4G_1)$ state and the second excitation is due to 6A_1 to ${}^4E, {}^4A_1({}^4G)$ ligand field transitions and the field transfer band tail [16]. These transitions get overlapped and form a broad region of absorption band. The absorption below 450 nm is associated with the charge transfer transition (d–d). The energy band gap at ~ 571 nm is associated with the metal to metal transitions while the band ~ 728 nm is associated with the crystal field transitions [17].

Fig. 4 (a) Magnetic hysteresis loop of BFO nanoparticles at room temperature, (b) temperature dependent magnetization curve of BFO nanoparticles, (c) room temperature frequency dependence of dielectric constant and dielectric loss and (d) temperature dependent dielectric constant of BFO nanoparticles



Band gap E_g for the direct band gap materials can be calculated by using the formula

$$\alpha h\nu = K(h\nu - E_g)^{1/2}$$

where K is a constant, E_g is the band gap and $h\nu$ is the photon energy. According to classical Tauc’s approach [18], the value of the band gap is estimated by extrapolating the linear portion of the graph intersecting X-axis at 0. Figure 3(d) shows $(\alpha E_{\text{photon}})^2$ versus E_{photon} curve based on the spectrum data of pure BFO nanoparticles. The energy band gap of BFO nanoparticles is estimated to be 2.17 eV which is in good agreement with the earlier reported band gap values for BFO nanoparticles [19] but this value of band gap is smaller as compared to BFO thin films [9]. This smaller value of the band gap indicates high ability of BFO nanoparticles to utilize visible light for the photocatalytic activities.

Figure 4(a) shows the magnetic hysteresis loop of BFO nanoparticles measured at room temperature, indicating ferromagnetic behavior. It is well known that bulk bismuth ferrite possesses cycloid spin of order 62 nm and no net magnetization at room temperature. The possible explanation which can describe the origin of net magnetization in nanoparticles of BFO ceramics could be its size dependent properties; As the particle size reduces, surface to volume ratio becomes very large which results in the structure distortion and the modification of the spiral G type antiferromagnetic ordering to the collinear G type antiferromagnetic structure in which the canted components becomes measurable. Further the cycloid spin structure is partly destroyed in BFO nanoparticles due to the average particle

size (30–50 nm) being less than that of cycloid spin order (62 nm). Figure 4(b) shows the temperature dependent magnetization of BFO nanoparticles. The magnetization increases slowly with decreasing temperature up to 50 K. The sharp increase in magnetization below 50 K indicates the ferromagnetic behavior of BFO nanoparticles at low temperature.

Figure 4(c) shows frequency dependence of dielectric constant and dielectric loss of BFO nanoparticles at room temperature. Dielectric constant and dielectric loss decreases slowly with increasing frequency in low frequency region and becomes frequency independent in high frequency region. This can be explained on the basis of dipole relaxation. High value of the dielectric constant at the low frequencies and low value of the dielectric constant at high frequencies indicates large dispersion due to the Maxwell-Wagner type of interfacial polarization in agreement with Koop’s phenomenological theory (the inability of the dipoles to follow the alternating field at high frequencies) [20, 21]. The variation of dielectric constant at various frequencies as a function of temperature is shown in Fig. 4(d). A dielectric anomaly in dielectric constant has been observed around $\sim 290^\circ\text{C}$ which could be related to antiferromagnetic Néel temperature (T_N). This type of behavior is also predicted by Landau-Devonshire theory of phase transition in magnetoelectrically ordered system as an influence of magnetic order on electric order. The appearance of dielectric anomaly around $\sim 290^\circ\text{C}$ which is well below the antiferromagnetic temperature (370°C) also indi-

cates the decrease in Néel temperature of BFO nanoparticles.

4 Conclusions

In summary, pure phase BFO nanoparticles were successfully synthesized by sol gel method via tartaric acid as a template material. XRD patterns confirmed distorted rhombohedral structure of BFO nanoparticles. XRD calculations and TEM micrographs revealed that the average crystallite/particle size varied in the range 30–50 nm. Raman spectroscopy also confirmed rhombohedral structure of BFO nanoparticles. FTIR studies showed the presence of Bi–O and Fe–O bonds in BFO samples sintered at 450 °C and 550 °C. BFO nanoparticles showed enhanced absorption of visible light with a broad absorption band (400–650 nm) indicating an energy band gap of 2.17 eV. Room temperature weak ferromagnetism and decrease in Néel temperature were observed for BFO nanoparticles. Pure phase BFO nanoparticles having improved ferromagnetic and enhanced optical properties in visible region may find potential applications in optoelectronic devices.

Acknowledgements This work was financially supported by Department of Science and Technology (DST) India through grant No. SR/FTP/PS-91/2009. Manisha Arora is thankful to IIIT Noida for providing Teaching Assistance.

References

1. Fiebig, M., Lottermoser, Th., Frohlich, D., Goltsev, A.V., Pisarev, R.V.: *Nature* **419**, 818 (2002)
2. Hill, N.A.: *J. Phys. Chem. B* **104**, 6694 (2000)
3. Fischer, P., Polomska, M., Sosnowska, I., Szymanski, M.: *J. Phys. C* **13**, 1931 (1980)
4. Wang, Y.P., Zhou, L., Zhang, M.F., Chen, X.Y., Liu, J.M., Liu, Z.G.: *Appl. Phys. Lett.* **84**, 1731 (2004)
5. Selbach, S.M., Tybell, T., Einarsrud, MA, Grande, T.: *Chem. Mater.* **19**, 6478 (2007)
6. Dai, H., Li, T., Xue, R., Chen, Z., Xue, Y.: *J. Supercond. Nov. Magn.* **25**, 109 (2012)
7. Tang, Y.H., Han, T.C., Liu, H.L., Lin, J.G.: *J. Supercond. Nov. Magn.* (2011). doi:10.1007/s10948-011-1257-7
8. Mazumder, R., Ghosh, S., Mondal, P., Bhattacharya, D., Dasgupta, S., Das, N., Sen, A., Tyagi, A.K., Sivakumar, M., Takami, T., Ikuta, H.: *J. Appl. Phys.* **100**, 033908 (2006)
9. Takahashi, K., Kida, N., Tonouchi, M.: *Phys. Rev. Lett.* **96**, 117402 (2006)
10. Gao, F., Chen, X., Yin, K., Dong, S., Ren, Z., Yuan, F., Yu, T., Zou, Z., Liu, J.M.: *Adv. Mater.* **19**, 2889 (2007)
11. Gao, F., Yuan, Y., Wang, K.F., Chen, X.Y., Chen, F., Liu, J.M.: *Appl. Phys. Lett.* **89**, 102506 (2006)
12. Fukumura, H., Matsui, S., Harima, H., Takahashi, T., Itoh, T., Kisoda, K., Tamada, M., Noguchi, Y., Miyayama, M.: *J. Phys. Condens. Matter* **19**, 365224 (2007)
13. Singh, M.K., Jang, H.M., Ryu, S., Jo, M.H.: *Appl. Phys. Lett.* **88**, 42907 (2006)
14. Yang, H., Xian, T., Wei, Z.Q., Dai, J.F., Jiang, J.L., Feng, W.J.: *J. Sol-Gel Sci. Technol.* **58**, 238 (2011)
15. Bhushan, B., Basumallick, A., Bandopadhyay, S.K., Vasanthacharya, N.Y., Das, D.: *J. Phys. D, Appl. Phys.* **42**, 065004 (2009)
16. Jaiswal, A., Das, R., Vivekanand, K., Abraham, P.M., Adyanthaya, S., Poddar, P.: *J. Phys. Chem. C* **114**, 2108 (2010)
17. Zhang, S.T., Lu, M.H., Wu, D., Chen, Y.F., Ming, N.B.: *Appl. Phys. Lett.* **87**, 262907 (2005)
18. Chang, D.A., Lin, P., Tseng, T.Y.: *J. Appl. Phys.* **77**, 4445 (1995)
19. Joshi, U.A., Jang, J.S., Borse, P.H., Lee, J.S.: *Appl. Phys. Lett.* **92**, 242106 (2008)
20. Maxwell, P.C.: *Electricity and Magnetism*, vol. 1. Oxford University Press, Oxford. Section 328
21. Koops, C.G.: *Phys. Rev.* **83**, 121 (1951)